

Genetic algorithm prediction of pressure-induced multiferroicity in the perovskite  $\text{PbCoO}_3$ Feng Lou,<sup>1,2</sup> Wei Luo,<sup>1,2</sup> Junsheng Feng,<sup>3</sup> and Hongjun Xiang<sup>1,2,\*</sup><sup>1</sup>Key Laboratory of Computational Physical Sciences (Ministry of Education), State Key Laboratory of Surface Physics, and Department of Physics, Fudan University, Shanghai 200433, People's Republic of China<sup>2</sup>Collaborative Innovation Center of Advanced Microstructures, Nanjing 210093, People's Republic of China<sup>3</sup>School of Physics and Materials Engineering, Hefei Normal University, Hefei 230601, People's Republic of China

(Received 30 November 2018; revised manuscript received 5 April 2019; published 3 May 2019)

It was well known that pressure can have profound effects on the structural, magnetic, and electronic properties of transition metal oxides. However, it is a challenge both experimentally and theoretically to determine the exact structural and magnetic order of a complicated oxide system under pressure. To this end, we develop a global optimization approach based on the genetic algorithm by taking into account explicitly both structural and magnetic degrees of freedom. With this approach, we investigate the effect of pressure on the structure, magnetism, and charge ordering of the recently synthesized perovskite oxide  $\text{PbCoO}_3$ , which is an interesting system since both Pb and Co sites can change the valence states. At low pressure, we predict that  $\text{PbCoO}_3$  can order in two multiferroic phases (i.e.,  $R3c$  and  $Pna2_1$ ). Both phases are ferroelectric with a large electric polarization due to unusual coupling between the ferroelectric mode and other antipolar modes. Both phases display weak ferromagnetism. The ferroelectric polarization and weak ferromagnetism in these two phases are coupled to each other, suggesting that they may be used to realize the electric field control of magnetism. At higher pressure, the valence transition takes place from  $\text{Pb}^{4+}\text{Co}^{2+}\text{O}_3$  to the  $A$ -site and  $B$ -site charge-ordering state  $\text{Pb}^{2+}\text{Pb}_3^{4+}\text{Co}_2^{3+}\text{Co}_2^{3+}\text{O}_{12}$  accompanied with an unusual enhancement of the band gap. In this work, we not only provide a general powerful method to determine the spin-orbital-charge ordering of intriguing correlated systems, but also predict that  $\text{PbCoO}_3$  may be a multiferroic material under low pressure.

DOI: [10.1103/PhysRevB.99.205104](https://doi.org/10.1103/PhysRevB.99.205104)

## I. INTRODUCTION

Perovskite oxides  $\text{ABO}_3$  are an important class of functional materials that have been studied for decades, given their exotic electronic and magnetic properties. In particular, transition metal perovskite oxides with lone-pair  $A$ -site cations (such as  $\text{Bi}^{3+}$  and  $\text{Pb}^{2+}$ ) are of great interest since some of them are important ferroelectric (e.g.,  $\text{PbTiO}_3$ ) [1] and multiferroic materials (e.g.,  $\text{BiFeO}_3$ ) [2]. Applying pressure has become a very useful technique for studying lone-pair  $A$ -site perovskite oxides. First, many lone-pair  $A$ -site perovskite oxides (e.g.,  $\text{BiCoO}_3$ ) [3] can only be synthesized at high pressure. Second, the application of pressure may lead to diverse intriguing properties and exotic phenomena, including enhancement of ferroelectric (FE) polarization [1], high-spin/low-spin transition [3,4], magnetic ordering transition [5], and insulator-to-metal transition [6–11]. Interesting and surprisingly, pressure may also induce intermetallic valence transition (i.e., charge-ordering transition) since the valence-skipping nature [12] of the lone-pair ion may result in either  $6s^2(\text{Bi}^{3+}, \text{Pb}^{2+})$  or the  $6s^0(\text{Bi}^{5+}, \text{Pb}^{4+})$  electronic configurations. For example, the valence transition from the  $A$ -site charge-ordering phase  $(\text{Pb}^{2+})_{0.5}(\text{Pb}^{4+})_{0.5}\text{Cr}^{3+}\text{O}_3$  to  $\text{Pb}^{2+}\text{Cr}^{4+}\text{O}_3$  takes place when the pressure is increased to about 2.5 GPa which is associated with a simultaneous insulator-to-metal transition [9].

Similarly, the pressure causes the valence transition from the insulating  $P\bar{1}$   $(\text{Bi}^{3+})_{0.5}(\text{Bi}^{5+})_{0.5}\text{Ni}^{2+}\text{O}_3$  phase to the metallic  $Pbnm$   $\text{Bi}^{3+}\text{Ni}^{3+}\text{O}_3$  phase [10,11].

Among the lone-pair  $A$ -site perovskite oxides,  $\text{PbCoO}_3$  is one of the most interesting and complicated compounds. Recently, perovskite  $\text{PbCoO}_3$  was successfully synthesized for the first time at a high pressure (above 12 GPa) [13]. In this high-pressure phase, there is a simultaneous  $A$ -site and  $B$ -site charge-ordering  $\text{Pb}^{2+}\text{Pb}_3^{4+}\text{Co}_2^{3+}\text{Co}_2^{3+}\text{O}_{12}$ . To our best knowledge, this is the only  $\text{ABO}_3$  system where a simultaneous  $A$ -site and  $B$ -site charge ordering occurs. It was suggested that this insulating phase adopted a nonpolar (space group  $Pn\bar{3}$ ) structure with a  $2 \times 2 \times 2$  supercell of the pseudocubic phase. However, several key issues for  $\text{PbCoO}_3$  remain to be clarified. First, what is the exact structure of the high-pressure phase, since it is very hard to accurately determine the oxygen positions under pressure? Second, how will the pressure affect the geometrical structure and charge-ordering/spin-ordering, since pressure may induce intermetallic valence transition? It is well known that many Pb- or Bi-based transition metal oxides (e.g.,  $\text{PbTiO}_3$  [1],  $\text{BiFeO}_3$  [2],  $\text{BiCoO}_3$  [4],  $\text{PbNiO}_3$  [14], and  $\text{PbVO}_3$  [15]) are ferroelectrics or multiferroics under ambient or low pressure. It will be interesting to see whether  $\text{PbCoO}_3$  becomes a multiferroic under low pressure. Therefore, a systematic investigation of  $\text{PbCoO}_3$  is highly desirable to clarify the phase diagram and the possible multiferroic behavior.

In this work, we first propose a global optimization approach based on the genetic algorithm to predict the

\*Corresponding author.

ground-state structures of magnetic systems and implement it in our material simulation and property calculation package (MSPCP) [16–20]. In this approach, we optimize structural and magnetic degrees of freedom simultaneously. Then, we predict the phase evolution in  $\text{PbCoO}_3$  as a function of hydrostatic pressure with our unique approach. We find that  $\text{PbCoO}_3$  under low pressure is both ferroelectric and weak ferromagnetic (i.e., multiferroic): The  $R3c$  phase has the lowest enthalpy between 0.5 GPa and 7.5 GPa; then the  $Pna2_1$  phase becomes the most stable for pressure up to 13 GPa. A phase transition from the non-charge-ordering  $\text{Pb}^{4+}\text{Co}^{2+}\text{O}_3$  phase to a simultaneous  $A$ -site and  $B$ -site charge-ordering  $\text{Pb}^{2+}\text{Pb}_3^{4+}\text{Co}_2^{2+}\text{Co}_2^{3+}\text{O}_{12}$   $P\bar{1}$  phase takes place at 13 GPa, in agreement with the experimental result [13].

## II. METHODS

### A. Genetic algorithm for magnetic systems

In the past, some global optimization algorithms were proposed to predict the ground state of three-dimensional crystals and layered materials [21–25]. The magnetic degree of freedom is essential for describing magnetic systems such as transition metal perovskite oxides, so in order to search ground-state structures of magnetic systems, here, we develop genetic-algorithm-based global optimization approaches which consider explicitly the magnetic degree of freedom. In our approaches, two different methods are proposed. In the first method [referred to as the full genetic algorithm (FGA) method], all structural and magnetic degrees of freedom are considered. In the second method [referred to as the perturbation genetic algorithm (PGA) method], the basic structural framework is fixed while the perturbation of the framework and magnetic degrees of freedom are optimized.

#### 1. Full genetic algorithm method

The genetic algorithm is a flexible evolutionary algorithm which originates from natural heredity, mutation, and selection. Since the genetic algorithms for structural searching were well documented in the literature [26], here we mainly provide the details of our FGA method that are relevant to the magnetic degree of freedom.

To generate the initial structures, we first randomly choose a space group and generate a random structure with this space group  $\mathbf{G}$ . Then we randomly choose a magnetic space group that is compatible with the given space group  $\mathbf{G}$ . The spin directions of the magnetic ions are set according to the chosen magnetic space group. For the system with variable valence ions (e.g.,  $\text{Co}^{2+}$  and  $\text{Co}^{3+}$ ), the spin magnitudes are also allowed to vary. Then, the spin moments are optimized in the density functional theory (DFT) calculations.

In the crossover process, we not only keep the geometrical information, but also keep spin moments in the same time. This is achieved by treating the atomic position and the associated spin moment as a whole in the cut-and-splice operation. For the mutation, the spin moment has a probability to be flipped. For the system with variable valence ions, the spin magnitudes has a probability to vary.

In order to increase the diversity of the structures, one needs to remove the similar structures. To check whether

two magnetic structures are similar, we first adopt the bond characterization matrix [22] to check whether the geometrical structure is the same or not. If the geometrical structures of these two magnetic structures are close to each other, we further check whether they have the same magnetic configuration.

### 2. Perturbation genetic algorithm method

The FGA method discussed above is powerful in that it can be used to search the lowest-energy structure of magnetic materials without giving any prior information. However, if the basic structural framework (e.g., perovskite) is known and the purpose is to find out the distortion (e.g., oxygen octahedron rotation) leading to the lowest energy, we propose an alternative method, i.e., the PGA method. By reducing the searching space, our PGA method is much more efficient than the FGA method in this case.

To generate an initial distorted structure, we first randomly select a subgroup  $\mathbf{G}$  of the space group  $\mathbf{G}_p$  of the high-symmetry parent structure (e.g., the  $Pm\bar{3}m$  perovskite structure). We then generate a random structure with the space group  $\mathbf{G}$  with the following procedure: (1) We add small perturbations (atomic displacements and strains) to the parent structure; (2) we symmetrize the random structure so that the space group of the resulting structure is  $\mathbf{G}$ ; (3) similar to the FGA method, we then set the spin moments according to a randomly chosen magnetic space group of the space group  $\mathbf{G}$ .

For the crossover process, we introduce an additional mating operation beside the traditional cut-and-splice method proposed by Deaven and Ho [27]. Since the distortion in the ground state is usually a superposition of different modes (e.g., there exist the octahedron rotation and FE displacement in the FE  $R3c$  phase of  $\text{BiFeO}_3$ ), we propose the following mating operation:  $X_{\text{child}} = X_{\text{orig}} + (X_{\text{father}} - X_{\text{orig}}) + c(X_{\text{mother}} - X_{\text{orig}})$ , where  $X_{\text{child}}$  represent the child structure,  $X_{\text{orig}}$  represents the original high-symmetry structure,  $X_{\text{father}}$  and  $X_{\text{mother}}$  represent the parent structures, and the constant  $c$  is randomly chosen to be 1 or  $-1$  so as to take the sum or difference between these two distortions. This is in the same spirit as the differential evolution algorithm [23].

In our GA simulations, the number of generations is set to be 20 and each generation includes a population of 20 individual structures. For each system, we repeat each simulation twice to check the reliability of our results.

### B. DFT calculation

In this work, the density functional theory (DFT) calculations are performed to relax the structures and calculate the energies on the basis of the projector augmented wave (PAW) [28] method encoded in the Vienna *ab initio* simulation package (VASP) [29]. The exchange-correlation energy is described by the Perdew-Burke-Ernzerhof (PBE) [30] functional of the generalized gradient approximation (GGA). The PAW potentials include 14 valence electrons for Pb ( $5d^{10}6s^26p^2$ ), nine for Co ( $3d^84s^1$ ), and six for oxygen ( $2s^22p^4$ ). Typical computational parameters for our calculations are a 600-eV plane-wave energy cutoff; an  $8 \times 8 \times 8$  (10 atoms),  $8 \times 8 \times 6$  (20 atoms), or  $6 \times 6 \times 6$  (40 atoms) Monkhorst-Pack  $k$ -point sampling mesh set; and a 0.01-eV/Å force tolerance for

structural relaxation calculations. The strong correlation effects of Co  $d$  electrons are included by means of the DFT +  $U$  scheme with a moderate value of  $U_{\text{eff}} = 4.0$  eV which meets well with the critical pressure of charge-ordering phase in the experiments. Our test calculations shows that other  $U$  values give similar phase diagrams (see Table S1 of the Supplemental Material (SM) [31]). To describe the electronic structure more accurately, we adopt the hybrid functional HSE06 [32] to calculate the density of states, band structure, and electric polarization. The polarization is calculated by the Berry phase method [33]. The dynamical stability is determined by phonon calculations as implemented in the PHONOPY code [34].

### III. RESULTS AND DISCUSSION

#### A. Benchmarks for the GA methods

We now check whether the FGA and PGA methods are able to reproduce the known phases of the perovskite oxide systems. First, we consider  $\text{BiFeO}_3$ , which is a room-temperature multiferroic with a  $G$ -type antiferromagnetic (AFM) spin order and the  $R3c$  space group [2]. Our tests show that the FGA method takes about 20 generations to find the lowest-energy spin order and structural order. As expected, the PGA method gives the ground state of  $\text{BiFeO}_3$  within five generations starting from the cubic perovskite structure. Therefore, our PGA method is highly efficient if the framework is known in prior. Second, the charge-ordering system  $\text{CaFeO}_3$  is selected as another example. At low temperature,  $\text{CaFeO}_3$  shows the valence transition from  $\text{Ca}^{2+}\text{Fe}^{4+}\text{O}_3$  to a  $G$ -type charge-ordering state  $\text{Ca}^{2+}(\text{Fe}^{3+})_{0.5}(\text{Fe}^{5+})_{0.5}\text{O}_3$  [35]. Our PGA method is able to predict the charge-ordering configuration ( $P2_1/n$  space group) within five generations. These benchmarks suggest that our GA methods are powerful in predicting not only the crystal structures but also the magnetic configurations.

#### B. Phase diagram of $\text{PbCoO}_3$ under hydrostatic pressure

To find out the lowest-enthalpy phases of  $\text{PbCoO}_3$  under different pressures, we first perform our FGA simulations at 0, 10, and 20 GPa to identify the basic framework of  $\text{PbCoO}_3$ . In these FGA simulations, the total number of atoms is set to be 20 (i.e., 4 formula units (f.u.)). The moderate value of Hubbard  $U_{\text{eff}} = 4.0$  eV is adopted to incorporate the strong correlation effects. At 0 and 10 GPa, our simulations shows that the ground-state structures have the perovskite framework and  $G$ -type magnetic configuration. At 20 GPa, a perovskite structure with the charge ordering of Co ions and ferromagnetic order (CO-FM) is found to be the most favorable. The lowest-enthalpy structures from our FGA simulations are shown in Fig. S1 of the Supplemental Material (SM) [31]. Therefore, our FGA simulations with the 20-atom supercell suggest that the framework of  $\text{PbCoO}_3$  should be perovskite from ambient pressure to 20 GPa. Then, we employ our PGA simulations to investigate systematically the ground-state structures under hydrostatic pressure from ambient pressure to 20 GPa with the interval of 2 GPa. In our PGA simulations, the supercell contains up to 40 atoms (i.e., 8 f.u.). In addition, we also perform FGA simulations with the 30-atom supercell. We find that the 30-atom hexagonal  $\text{YMnO}_3$ -type structure is the

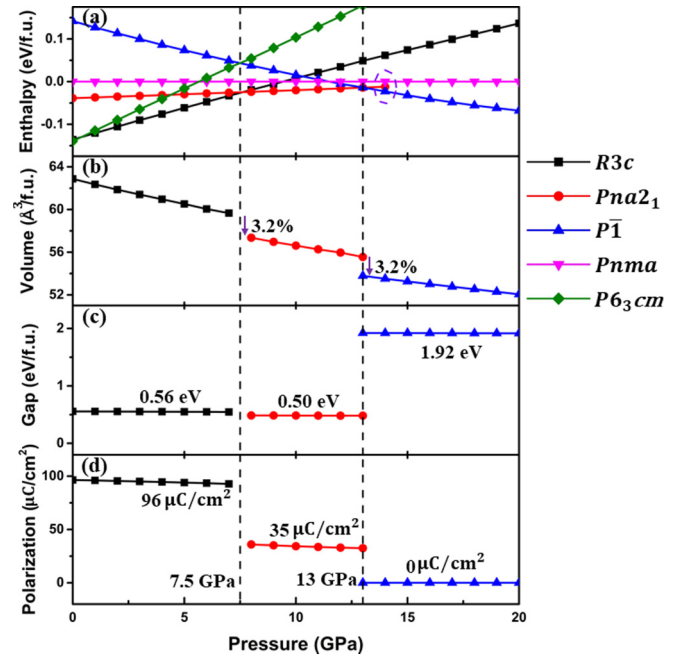


FIG. 1. The evolution of enthalpy, volume, gap, and electric polarization as the function of hydrostatic pressure for different  $\text{PbCoO}_3$  phases. (a) The calculated enthalpy as a function of pressure. The enthalpy of the  $Pnma$  phase is taken as the reference. The violet dotted circle denotes that the polar  $Pna2_1$  structure automatically evolves into the centrosymmetric  $Pnma$  structure under higher pressure (about 14 GPa). (b) The calculated volume as the function of pressure. The violet arrows denote the sharp drop of the volume. (c) The calculated band gap as a function of pressure. One can see that the  $P\bar{1}$  phase has an unusually large band gap. (d) The calculated electric polarization as a function of the pressure. As the pressure increases, the polarization decreases.

ground state from 0 to 0.5 GPa while the perovskite structure is preferred from 0.5 to 20 GPa. The calculated phase diagram, the dependence of volume, band gap, and polarization on pressure are summarized in Fig. 1. To further check our results, we also consider some other known  $\text{ABO}_3$  structures (e.g., postperovskites and hexagonal manganite) which do not have the perovskite motif (See Fig. S2 of the SM [31]).

From Fig. 1, we can see that at ambient pressure, the ground state is a hexagonal  $\text{YMnO}_3$ -type structure with the polar space group  $P6_3cm$ . However, the pressure range (0–0.5 GPa) in which the  $P6_3cm$   $\text{PbCoO}_3$  phase has the lowest enthalpy is rather narrow. In fact, the  $\text{LiNbO}_3$ -type  $R3c$   $\text{PbCoO}_3$  phase lies 0.004 eV/f.u. higher in energy than the  $P6_3cm$  phase at ambient pressure. The  $R3c$  phase becomes the ground state as the pressure increases to 0.5 GPa. In addition, we find that the stability of the  $P6_3cm$  phase decreases with the increase of the Hubbard  $U$  value  $U_{\text{eff}}$ . If  $U_{\text{eff}} = 5.0$  eV is adopted, the  $R3c$  phase becomes the ground state at ambient pressure (see Table S1 of the SM [31]). These results suggest that the  $P6_3cm$  phase might be hard to synthesize; thus we will not discuss this phase hereafter.

Between 0.5 and 7.5 GPa, the  $R3c$  phase has the lowest enthalpy. The  $R3c$  phase is isostructural to the well-known multiferroics  $\text{BiFeO}_3$  [2] and  $\text{PbNiO}_3$  [14]. The primitive unit cell of the  $R3c$  phase contains 2 f.u. (ten atoms) due to the



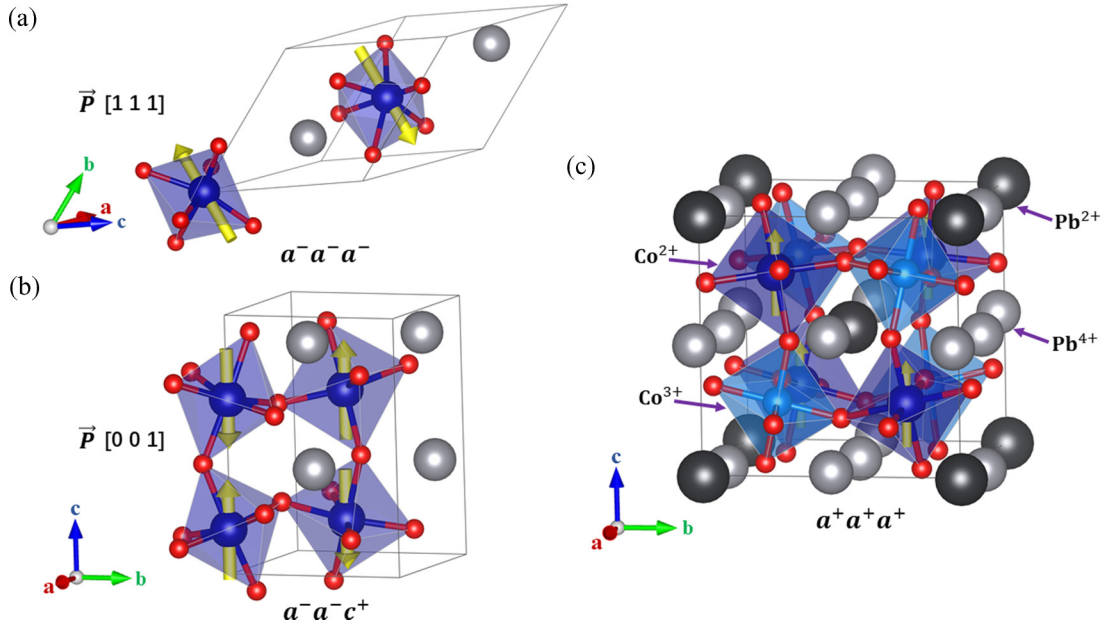


FIG. 2. The ground-state structures of  $\text{PbCoO}_3$  under different pressure. (a) The polar  $\text{LiNbO}_3$ -type structure  $R3c$  under pressure from 0.5 to 7.5 GPa. (b) The polar  $Pna2_1$  phase under pressure from 7.5 to 13 GPa. (c) The A-site and B-site charge-ordering  $P\bar{1}$  phase under pressure from 13 to 20 GPa. The yellow arrows represent the directions of magnetic moments. The small canting of moments in the  $R3c$  and  $Pna2_1$  phases is not shown here.

counter-rotations of neighboring O octahedra about the  $[111]$  axis (i.e.,  $a^-a^-a^-$  in Glazer's notation) [36] [see Fig. 2(a)]. The  $R3c$  phase has a large FE polarization along the  $[111]$  axis mainly due to the displacement of the Pb ions.

Between 7.5 and 13.0 GPa, another polar phase with the  $Pna2_1$  space group becomes the ground state. The primitive unit cell of the  $Pna2_1$  phase contains 4 f.u. (20 atoms). The  $a^-a^-c^+$  octahedron tilt system is similar to that in the  $Pbnm$   $\text{GdFeO}_3$ -type structure [see Fig. 2(b)]. The FE polarization of the  $Pna2_1$  phase is along the  $[001]$  direction, different from the  $R3c$  case.

When the pressure is increased to 13 GPa, a phase transition from the polar  $Pna2_1$  phase to the nonpolar  $P\bar{1}$  phase takes place. The  $P\bar{1}$  phase is a complicated perovskite structure. Its primitive unit cell contains 8 f.u. (40 atoms). The octahedron rotation adopts the uncommon  $a^+a^+a^+$  tilt system [see Fig. 2(c)]. As we will discuss later in detail, the  $P\bar{1}$  phase adopts a simultaneous A-site and B-site charge ordering  $\text{Pb}^{2+}\text{Pb}^{4+}\text{Co}^{2+}\text{Co}^{3+}\text{O}_{12}$ , in agreement with the experimental finding [13].

All three  $\text{PbCoO}_3$  phases ( $R3c$ ,  $Pna2_1$ , and  $P\bar{1}$ ) are found to be insulating (see Fig. 3). Note that all these three phases are locally stable under ambient pressure [see Fig. 1(a)]. Interestingly, the  $P\bar{1}$  phase at higher pressure has a much larger band gap (1.9 eV vs 0.5 eV) than the other two phases [see Fig. 1(c)]. Structure parameters for these phases are summarized in Tables S6, S7, and S9 of the SM [31]. In the following, we will discuss the physical properties of these three phases in detail.

### C. Multiferroic $R3c$ phase with a high polarization

First we discuss the valence states of the Pb and Co ions in the  $R3c$  phase. The partial density of states (DOS) is shown

in Fig. 3(b). We can see that a significant portion of the Pb 6s states is unoccupied, indicating that the Pb ion adopts the +4 valence state. This is because the 6s states of a  $\text{Pb}^{2+}$  ion would be almost fully occupied [see Fig. 3(a)]. Therefore, the Co ion would adopt the +2 valence state in the  $R3c$  phase in order to satisfy the charge balance. Indeed, the local magnetic moment for the Co ion is computed to be  $2.7 \mu_B$ , which is close to the value ( $3 \mu_B$ ) of the high-spin  $d^7$   $\text{Co}^{2+}$  ion. Thus, the  $R3c$  phase adopts the  $\text{Pb}^{4+}\text{Co}^{2+}\text{O}_3$  valence state.

The  $R3c$   $\text{PbCoO}_3$  phase displays a rather high FE polarization of  $96.5 \mu\text{C}/\text{cm}^2$  at ambient pressure [see Fig. 1(d)], which is close to that in the well-known multiferroic  $\text{BiFeO}_3$ . However, the ferroelectricity in the  $R3c$   $\text{PbCoO}_3$  phase is not due to the lone-pair mechanism since the  $\text{Pb}^{4+}$  ion has no lone-pair electron, in contrast to the  $\text{Bi}^{3+}$  ion in  $\text{BiFeO}_3$ . In order to reveal the FE mechanism in the  $R3c$   $\text{PbCoO}_3$  phase, we perform the mode decomposition for the  $R3c$   $\text{PbCoO}_3$  phase with respect to the cubic paraelectric phase. As expected, there are two dominant modes, i.e., the octahedron rotation with the irreducible representation (irrep)  $R_5^-$  and the A-site FE displacement with the irrep  $\Gamma_4^-$  [see Fig. 4(a)]. Due to the presence of the  $R_5^-$  rotation mode, the octahedral tilt system can be represented by  $a^-a^-a^-$ . The dynamical stability of the  $R3c$  phase is confirmed by phonon calculations. The total energy is computed as a function of the amplitude of FE  $\Gamma_4^-$  and rotation  $R_5^-$  modes relative to the parent cubic structure, as shown in Fig. 4(b). We can see a double-well potential for both the rotation mode and the FE displacement mode. Since the FE mode itself is unstable, the ferroelectricity in the  $R3c$   $\text{PbCoO}_3$  phase may be classified to be the proper type. The instability of the A-site FE mode is due to the small radius of the  $\text{Pb}^{4+}$  ion (the tolerance factor of  $\text{Pb}^{4+}\text{Co}^{2+}\text{O}_3$  is estimated to be 0.825), similar to the case of  $\text{LiOsO}_3$  [37] and  $\text{ZnSnO}_3$  [38]. However, the FE displacement at the energy

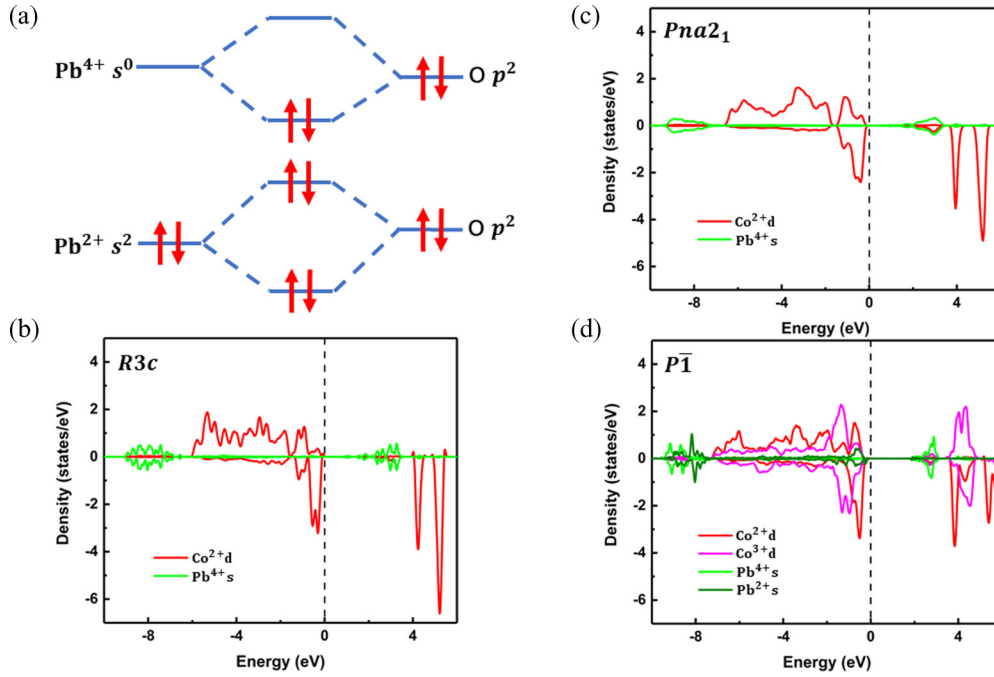


FIG. 3. Electronic structures of different  $\text{PbCO}_3$  phases. (a) Schematic illustration of the chemical bonding of two different Pb ions. For the  $\text{Pb}^{4+}$  ion, some  $6s$  states are unoccupied while for  $\text{Pb}^{2+}$  ions, almost all the  $6s$  states are fully occupied. (b) The total and atom-resolved density of states (DOS) of the  $R3c$  phase at ambient pressure. (c) DOS of the  $Pna2_1$  phase at 8 GPa. (d) DOS of the  $P\bar{1}$  phase at 16 GPa. In  $R3c$  and  $Pna2_1$ , we can see that a significant portion of the Pb  $6s$  states is not occupied, indicating that the Pb ion adopts the +4 valence state. In other word, these two phases adopt the  $\text{Pb}^{4+}\text{Co}^{2+}\text{O}_3$  valence state. In  $P\bar{1}$ , there are two kinds of Pb ions and two kinds of Co ions. The Pb ions with almost fully occupied  $6s$  states adopt the +2 valence state, and the other Pb ions with a significant portion of unoccupied of Pb  $6s$  states still keep the +4 valence state. Considering the number ratio of these ions, the  $P\bar{1}$  phase displays the simultaneous  $A$ -site and  $B$ -site charge ordering in the form of  $(\text{Pb}^{2+})_{0.25}(\text{Pb}^{4+})_{0.75}(\text{Co}^{2+})_{0.5}(\text{Co}^{3+})_{0.5}\text{O}_3$ . In the DOS calculation for the  $R3c$  and  $Pna2_1$  phases, the  $G$ -AFM spin configuration is adopted. In  $P\bar{1}$ , the charge-ordered FM spin configuration is adopted.

minimum due to the sole presence of the FE mode is only 65% of the total FE displacement in the fully relaxed  $R3c$  phase. Interestingly, it is the presence of the strong rotation mode that enlarges the energy gain of the FE displacement and enhances the FE polarization [see Fig. 4(b)]. This is an unusual case where the ferroelectricity is enhanced rather than suppressed by the octahedron rotation, as was reported in the  $\text{ZnSnO}_3$  system [38]. We note that the rotation angle ( $\sim 20^\circ$ ) of the octahedron in the  $R3c$   $\text{PbCoO}_3$  phase is close to that ( $\sim 19^\circ$ ) in  $\text{ZnSnO}_3$ . It was proposed that the negative  $-u^2R^4$  term instead of the usual positive  $u^2R^2$  term is responsible for this phenomenon. The  $-u^2R^4$  is also evident from the pressure behavior of the FE polarization and the rotation amplitude. As shown in Fig. 4(c), the pressure suppresses the octahedron rotation and the FE polarization. The pressure behavior of the octahedron rotation is expected since the pressure usually weakens the octahedron rotation in the  $\text{ABO}_3$  perovskite with a high-valence  $A$  ion [39]. The FE polarization is then also suppressed by pressure since the octahedron rotation angle becomes smaller. Therefore, the  $R3c$   $\text{PbCoO}_3$  phase is an unusual proper ferroelectric with the ferroelectricity greatly enhanced by the strong octahedron rotation.

For the magnetic ground state, our collinear density functional theory calculation shows that the  $G$ -type checkboard AFM state has the lowest energy (see Table S2 of the SM [31]). With the energy mapping approach [40], the nearest-neighbor symmetric exchange interaction  $J$  is computed to be

7.5 meV. Here, the spin interaction parameters are effective by setting the spin values of  $\text{Co}^{2+}$  to 1. By performing the parallel tempering Monte Carlo (PTMC) simulation with the MSPCP code, the Néel temperature is estimated to be 284 K (see Fig. S4(a) of the SM [31]). After taking into account the spin-orbit coupling effect, we find that the local spin moments tend to be perpendicular to the FE polarization; i.e., they tend to be in the (111) plane. If we define the AFM order parameter  $\mathbf{L}$  to be  $\mathbf{L} = \mathbf{M}_1 - \mathbf{M}_2$  ( $\mathbf{M}_1$  and  $\mathbf{M}_2$  are the magnetization of the two Co sublattices of the  $R3c$  phase), we will have  $\mathbf{L} \perp \mathbf{P}$ . Interestingly, there is a net canting spin moment  $\mathbf{M} = \mathbf{M}_1 + \mathbf{M}_2$  (about  $0.014 \mu\text{B}/\text{f.u.}$ ) due to the Dzyaloshinskii-Moriya (DM) interaction [41,42]. The canting moment  $\mathbf{M}$  is found to be perpendicular to both  $\mathbf{L}$  and  $\mathbf{P}$ . Since  $\mathbf{P}$  is in the same direction as the tilt mode  $\mathbf{R}_5^-$ , the direction of  $\mathbf{M}$  can be explained in terms of the  $\mathbf{R}_5^- \cdot (\mathbf{L} \times \mathbf{M})$  coupling proposed by Bellaiche *et al.* [43].

Since the  $R3c$   $\text{PbCoO}_3$  phase is both FE and weakly ferromagnetic, one can regard it as a multiferroic material. There is also a magnetoelectric (ME) coupling between the FE polarization and the weak ferromagnetism. Because of the cubic symmetry of the parent cubic perovskite structure, there are eight symmetrically equivalent [111] directions. Thus, there might occur eight different FE domains. Our test calculations show that the weak ferromagnetism is always perpendicular to the polarization direction. Therefore, a  $71^\circ$  or  $109^\circ$  switch of FE domains by the electric field will change

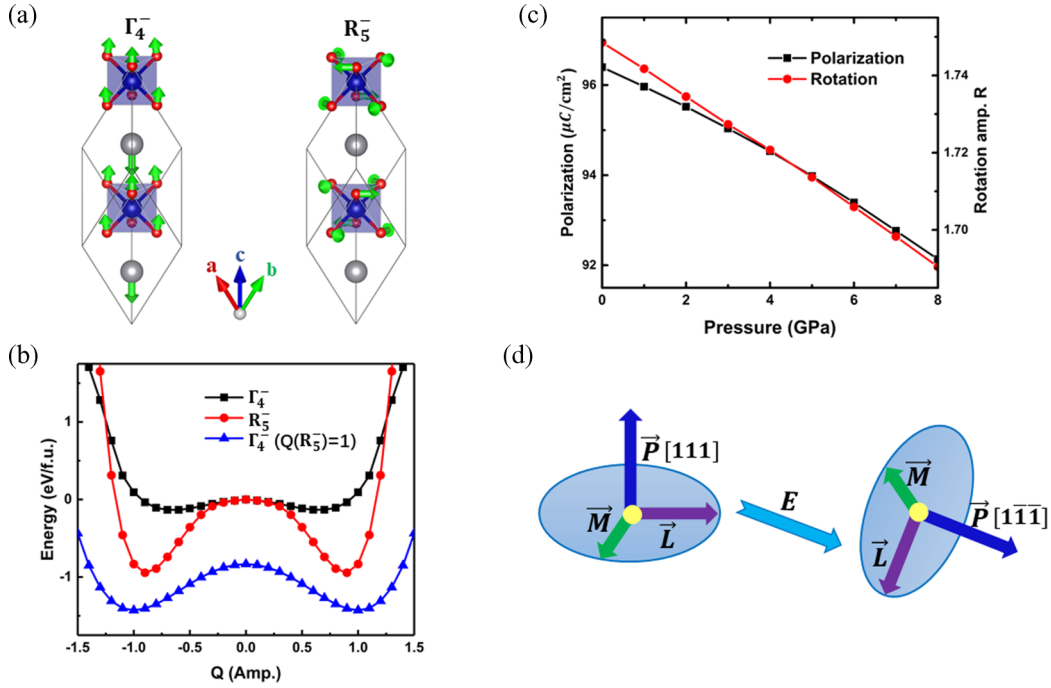


FIG. 4. Ferroelectric property and magnetoelectric coupling of the  $R3c$  phase. (a) Schematic illustration of the FE mode ( $\Gamma_4^-$ ) and oxygen octahedral rotation mode ( $R_5^-$ ) relative to the cubic paraelectric state. The green arrows represent the direction of displacements. (b) Total energies per unit cell as a function of the amplitude ( $Q$ ) for  $\Gamma_4^-$  (black) and  $R_5^-$  (red) modes. (c) Amplitudes of polarization and rotation as a function of pressure. In these calculations, the ambient pressure condition is considered. (d) Schematic illustration of magnetoelectric (ME) coupling. A  $71^\circ$  or  $109^\circ$  switch of FE domains by the external electric field will be associated with the reorientation of the easy-plane magnetization.  $\vec{P}$ ,  $\vec{M}$ , and  $\vec{L}$  denote polarization, canting moment, and antiferromagnetic order parameter, respectively.

the orientation of the canting magnetization  $\vec{M}$ , as shown schematically in Fig. 4(d).

#### D. Multiferroic $Pna2_1$ phase with an unusual quadrilinear coupling

As can be seen from the partial DOS plot [see Fig. 3(c)], the Pb ion and the Co ion adopt +4 and +2 valence states in the  $Pna2_1$   $\text{PbCoO}_3$  phase, respectively. Thus, the  $Pna2_1$  phase adopts the  $\text{Pb}^{4+}\text{Co}^{2+}\text{O}_3$  valence state, similar to the  $R3c$   $\text{PbCoO}_3$  case.

As we mentioned above, the  $Pna2_1$   $\text{PbCoO}_3$  phase is FE with the polarization along the  $[001]$  axis. With the Berry phase method, the polarization is calculated to be about  $37 \mu\text{C}/\text{cm}^2$  (at 8 GPa) which decreases slightly with the increase of pressure [Fig. 1(d)]. Similar to the  $R3c$  phase, the ferroelectricity in the  $Pna2_1$  phase is not due to the lone-pair mechanism. To reveal the FE mechanism in the  $Pna2_1$  phase, we perform the mode decomposition and investigate the mode interactions. We find that there are five different dominant distortions: the FE displacement mode with irrep  $\Gamma_4^-$  [see Fig. 5(a)], the in-plane oxygen octahedral rotation mode with irrep  $M_2^+$  [see Fig. 5(b)], the out-of-plane oxygen octahedral tilt mode with irrep  $R_5^-$  [see Fig. 5(c)], the in-plane antiferroelectric (AFE) displacement mode with irrep  $X_5^+$  [see Fig. 5(d)], and the out-of-plane AFE displacement mode with irrep  $X_5^-$  [see Fig. 5(e)]. Due to the presence of  $M_2^+$  and  $R_5^-$  rotation modes, the octahedral tilt system can be represented by  $a^-a^-c^+$ . The dynamical stability of the  $Pna2_1$  phase is con-

firmed by phonon calculations. We compute the total energy as a function of the amplitude of individual  $\Gamma_4^-$ ,  $R_5^-$ ,  $X_5^+$ , and  $X_5^-$  modes relative to the parent cubic structure (see Fig. S5(a) of the SM [31]). Obviously, the rotation modes  $M_2^+$  and  $R_5^-$  are unstable as indicated by the double-well potential while the  $X_5^+$  and  $X_5^-$  AFE modes are stable modes with single-well potentials. As shown in the inset of Fig. 5(f), the FE  $\Gamma_4^-$  mode itself is unstable, while the energy lowering due to the FE mode is small (0.025 eV/f.u.). Our further analysis (see Fig. S5 of the SM [31]) demonstrates that an unusual quadrilinear coupling  $E \propto \alpha Q(M_2^+)Q(R_5^-)Q(X_5^+)Q(\Gamma_4^-)$  would stabilize the FE displacement significantly. The  $\alpha$  is a negative coefficient and  $Q$  denotes the amplitude of these modes. The energy lowering of the FE mode now becomes 0.60 eV/f.u. Therefore, we can draw the conclusion that the  $Pna2_1$  phase is an unusual ferroelectric in which the ferroelectricity is enhanced by a special quadrilinear coupling. Previously, it was proposed that the third-order trilinear coupling (i.e., the  $PR_1R_2$  coupling between FE mode  $P$  and two rotation modes  $R_1$  and  $R_2$ ) and the fourth-order coupling (i.e., the  $PR^3$  coupling between the FE mode  $P$  and a rotation mode  $R$ ) will give rise to the improper ferroelectricity in  $\text{Ca}_3\text{Mn}_2\text{O}_7$  [44] and  $\text{YMnO}_3$  [45], respectively. The  $Pna2_1$   $\text{PbCoO}_3$  phase is an example where the fourth-order quadrilinear coupling is found to play an important role in the ferroelectricity.

Similar to the  $R3c$  phase, the  $Pna2_1$  phase adopts a  $G$ -type AFM magnetic ground state if the spin-orbit coupling is neglected (see Table S2 of the SM [31]). With the energy mapping approach, the nearest-neighbor symmetric exchange

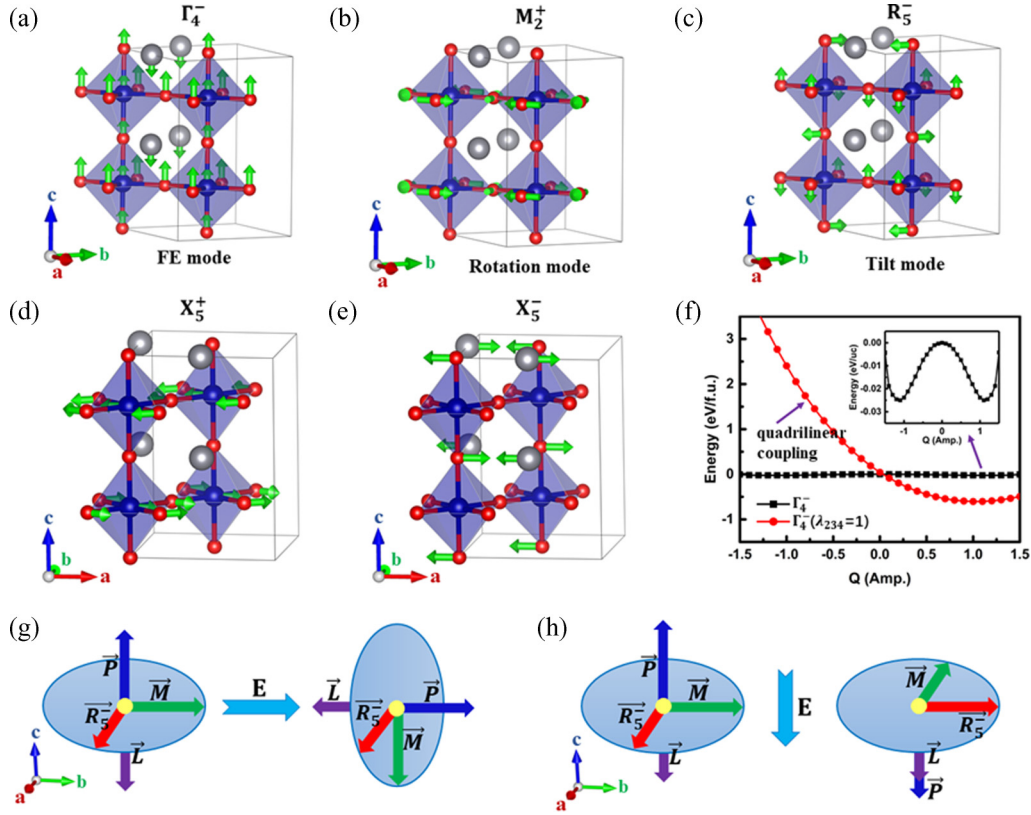


FIG. 5. Ferroelectric property and magnetoelectric coupling of the  $Pna2_1$  phase. (a)–(e) Different normal modes from the mode decomposition of the  $Pna2_1$  phase with respect to the cubic phase. The green arrows represent the direction of distortions. There are five distinct atomic distortions: (a) FE displacement mode related to the Pb ion with irrep  $\Gamma_4^-$ ; (b) in-plane oxygen octahedral rotation mode about the [001] axis with irrep  $M_2^+$ ; (c) in-plane oxygen octahedral tilt mode about the [100] axis with irrep  $R_5^-$ ; (d) in-plane AFE displacement mode with irrep  $X_5^+$ ; (e) out-of-plane AFE displacement mode with irrep  $X_5^-$ . (f) The quadrilinear coupling between the FE mode and the other three normal modes.  $\lambda_{234} = 1$  depicts  $Q(M_2^+) = 1$ ,  $Q(R_5^-) = 1$ , and  $Q(X_5^+) = 1$ . The calculations are performed at 8 GPa. (g), (h) Schematic illustration of magnetoelectric (ME) coupling. A  $90^\circ$  (g) or  $180^\circ$  (h) switch of FE domains by the external electric field may be associated with the reorientation of the canting magnetization.  $\mathbf{P}$ ,  $\mathbf{M}$ , and  $\mathbf{L}$  denote polarization, canting moment, and antiferromagnetic order, respectively.  $\mathbf{R}_5^-$  denotes the rotation axis of the  $R_5^-$  mode.

interaction  $J$  is computed to be 10.7 meV. Here, the spin interaction parameters are effective by setting the spin values of  $\text{Co}^{2+}$  to 1. The PTMC simulations indicate that the  $T_N$  of the  $Pna2_1$  phase is about 388 K (see Fig. S4(b) of the SM [31]). After the spin-orbit coupling is taken into account, the AFM order parameter  $\mathbf{L}$  tends to align along the  $c$  axis, i.e., the FE polarization direction. Interestingly, the DM interactions give rise to a small canting magnetic moment  $\mathbf{M}$  about  $0.013 \mu\text{B}/\text{f.u.}$  along one of the in-plane directions.

As we discussed above, the  $Pna2_1$   $\text{PbCoO}_3$  phase is FE with a large polarization and a high energy difference between the FE state and the cubic phase, and it has a high Néel temperature with a weak ferromagnetism. Therefore, the  $Pna2_1$   $\text{PbCoO}_3$  phase could be a high-temperature multiferroic material. We now investigate the possible ME coupling in this  $Pna2_1$  phase. Due to the cubic symmetry of the undistorted perovskite structure, the FE polarization can be along one of the three cubic directions (i.e., [100], [010], [001]). When the FE polarization is parallel or antiparallel to one (e.g., [001]) of the three cubic directions, there are four possible FE domains with the  $Pna2_1$  space group (see

Fig. S6 of the SM [31]). The order parameters in these domains are listed in Table S3 of the SM [31]. For each FE domain, the AFM order parameter  $\mathbf{L}$  is always parallel or antiparallel to the FE polarization  $\mathbf{P}$ , while the canting magnetic moment  $\mathbf{M}$  is always perpendicular to  $\mathbf{P}$ . Similar to the  $R3c$   $\text{PbCoO}_3$  case, the direction of the canting magnetic moment  $\mathbf{M}$  may be manipulated when the FE polarization  $\mathbf{P}$  is switched by  $90^\circ$  under an external electric field [see Fig. 5(g)]. Furthermore, there may exist another ME coupling for a  $180^\circ$  switch of the FE polarization  $\mathbf{P}$ . As can be seen from Table S3 of the SM [31], the reversal of the  $\Gamma_4^-$  FE mode can be achieved in two different ways: (1) the  $R_5^-$  mode remains unchanged; (2) the  $R_5^-$  mode changes the direction from  $\mathbf{a}$  to  $\mathbf{b}$ . Interestingly, in the case where the octahedral tilt  $R_5^-$  mode changes the direction when the FE polarization is reversed, the reversal of the FE polarization might result in a change of the canting magnetic moment  $\mathbf{M}$  [see Fig. 5(h)]. This can be understood with the  $\mathbf{R}_5^- \cdot (\mathbf{L} \times \mathbf{M})$  coupling: [43] The domain I ( $\mathbf{P} \parallel \mathbf{c}$ ,  $\mathbf{L} \parallel -\mathbf{c}$ ,  $\mathbf{R}_5^- \parallel \mathbf{a}$ , and  $\mathbf{M} \parallel \mathbf{b}$ ) has the same coupling energy as the domain IV ( $\mathbf{P} \parallel -\mathbf{c}$ ,  $\mathbf{L} \parallel -\mathbf{c}$ ,  $\mathbf{R}_5^- \parallel \mathbf{b}$ , and  $\mathbf{M} \parallel -\mathbf{a}$ ).



### E. Nonpolar $P\bar{1}$ phase with a simultaneous A-site and B-site charge ordering

The high-pressure  $P\bar{1}$   $\text{PbCoO}_3$  phase is much more complicated than the low-pressure  $R3c$  and  $Pna2_1$  phases. As can be seen from a partial DOS plot [see Fig. 3(d)] of the  $P\bar{1}$  phase, there are two kinds of Pb ions and two kinds of Co ions. One-fourth of the Pb ions now adopt the +2 valence state with almost fully occupied 6s states, and the other Pb ions still keep the +4 valence state. For the B sites, there are an equal number of  $\text{Co}^{2+}$  and  $\text{Co}^{3+}$  ions, which order in a checkerboard G-type manner [see Fig. 2(c)]. The  $\text{Co}^{3+}$  ions are in the low-spin nonmagnetic electronic configuration while the  $\text{Co}^{2+}$  ions adopt the high-spin electronic configuration. Our calculated local magnetic moment within the  $\text{Co}^{2+}$  sphere is  $2.61 \mu_B$  which is close to the result ( $2.6 \mu_B$ ) reported by Sakai *et al.* [13]. The charge disproportionation of Co can be observed in the breathing distortion of the oxygen octahedra where the oxygen octahedra with  $\text{Co}^{2+}$  have a larger volume than that of  $\text{Co}^{3+}$  by about 21%. The charge ordering of Co ions greatly lowers the total enthalpy by about 0.2 eV/f.u. (see Table S4 of the SM [31]). Thus, the  $P\bar{1}$  phase displays a simultaneous A-site and B-site charge ordering in the form of  $\text{Pb}^{2+}\text{Pb}_3^{4+}\text{Co}_2^{2+}\text{Co}_2^{3+}\text{O}_{12}$ , in agreement with the experimental result [13]. Note that the  $P\bar{1}$   $\text{PbCoO}_3$  phase is different from the A-site charge-ordering  $(\text{Bi}^{3+})_{0.5}(\text{Bi}^{5+})_{0.5}\text{Ni}^{2+}\text{O}_3$   $P\bar{1}$  phase [10,11].

The insulator behavior observed in the experiment (see Ref. [13]) is confirmed by our band structure calculations. Interestingly, the high-pressure  $P\bar{1}$  phase has a rather large band gap of 1.92 eV, which is even much larger than those (about 0.5 eV) of the low-pressure  $R3c$  and  $Pna2_1$  phases [see Fig. 1(c)]. This is quite uncommon since usually the band gap decreases with the increase of the pressure due to the shortened atomic distances and enhanced electron hopping [6–11]. It was discovered that the sodium that is metallic at ambient pressure will become insulating at 200 GPa [46]. This was attributed to the *p-d* hybridizations of valence electrons and their repulsion by core electrons into the lattice interstices when pressure is sufficiently high that atomic cores start to overlap strongly. In the  $P\bar{1}$   $\text{PbCoO}_3$  case, the transition pressure (13 GPa) is much lower, indicating that a different mechanism is playing a role. We note that there is a charge ordering in high-pressure  $P\bar{1}$   $\text{PbCoO}_3$  phase, in contrast to the low-pressure  $R3c$  and  $Pna2_1$  phases. As in other mixed valence materials, the metal-to-insulator transition is found to be associated with the emergence of charge ordering [8,10,11,35,47]. The carriers are localized and the material becomes more insulating when charges are distributed in a certain pattern rather than fluctuating with time at each site [48]. As can be seen from Fig. S3 of the SM [31], the small band gaps of the  $R3c$  and  $Pna2_1$  phases are due to the large dispersion of the conduction band minimum (CBM) dominated by the  $\text{Pb}^{4+}$  6s states. On the contrary, the unoccupied  $\text{Pb}^{4+}$  6s states of the  $P\bar{1}$  phase are much more localized since the interactions between the  $\text{Pb}^{4+}$  ions are largely blocked by the presence of the  $\text{Pb}^{2+}$  ions [see Fig. 2(c)]. Our study suggests that the discontinuous increase of the band gap with pressure is due to a unique pressure-induced charge-ordering mechanism.

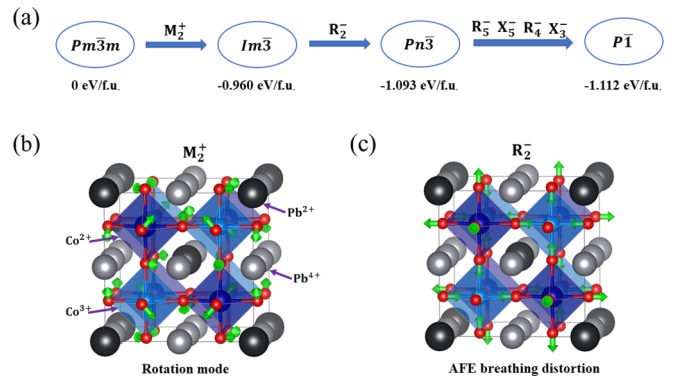


FIG. 6. Evolution of the  $P\bar{1}$  phase from the cubic phase. (a) Transition path from the cubic phase to the  $P\bar{1}$  phase. The calculations are performed at 16 GPa. The  $Pn\bar{3}$  and  $P\bar{1}$  phases have two common dominant distortions: (b) oxygen octahedral rotation mode with irrep  $M_2^+$  (c) AFE breathing distortion of the oxygen octahedra with irrep  $R_2^-$  which is related to the charge ordering of the Co ions. In the  $P\bar{1}$  phase, there are four additional small modes ( $R_5^-$ ,  $X_5^-$ ,  $R_4^-$ , and  $X_3^-$ ; see Fig. S8 of the SM [31]).

It was suggested that  $\text{PbCoO}_3$  adopts the  $Pn\bar{3}$  phase [13], which is slightly different from the  $P\bar{1}$  phase from our GA result (see Fig. S7 of the SM [31]). In Ref. [13], the experiment proposed the  $Pn\bar{3}$  structure to fit the synchrotron X-ray diffraction (SXRD) and electron diffraction (ED) patterns, and their theoretical calculations predicted that the structure with the  $R\bar{3}$  symmetry has lower enthalpy than the  $Pn\bar{3}$  structure. In our study, the genetic algorithm simulations show that the  $P\bar{1}$  structure is more stable than both the  $Pn\bar{3}$  and  $R\bar{3}$  phases (see Tables S4 and S5 of the SM [31]). The transition path from the cubic phase to the  $P\bar{1}$  phase is illustrated in Fig. 6(a). Our calculation indicates that the  $P\bar{1}$  phase has a lower enthalpy than the  $Pn\bar{3}$  phase (about 0.019 eV/f.u. at 16 GPa). Our predicted  $P\bar{1}$  phase is also more stable than the theoretically proposed low-energy  $R\bar{3}$  phase (see Ref. [13]) by 0.006 eV/f.u. The  $P\bar{1}$  phase has some features in common with the  $Pn\bar{3}$  phase: (1) The charge-ordering pattern is the same; (2) they have similar DOS distribution and band structure; (3) both phases display the unusual  $a^+a^+a^+$  tilt pattern associated with the  $M_2^+$  octahedral rotation mode [see Fig. 6(b)]; (4) there is an AFE breathing distortion of oxygen octahedra with irrep  $R_2^-$  in both phases [see Fig. 6(c)]. However, there are four additional modes with the irrep:  $R_5^-$ ,  $X_5^-$ ,  $R_4^-$ , and  $X_3^-$  in the  $P\bar{1}$  phase (see Fig. S8 of the SM [31]). Our calculations show that the sole presence of the  $R_5^-$ ,  $X_5^-$ ,  $R_4^-$ , or  $X_3^-$  mode is unfavored for the  $Pn\bar{3}$  phase. However, the combination of these four modes will significantly lower the total energy. Comparing with the  $Pn\bar{3}$  structure, the  $P\bar{1}$  phase is slightly distorted with a rhombohedral distortion and antiparallel displacements of Pb cations, which will account for the similar physical properties. We note that the density functional theory calculations are performed at zero temperature (0 K) while the experiment data of Ref. [13] are collected at room temperature (RT). At room temperature,  $\text{PbCoO}_3$  under high pressure might indeed adopt the  $Pn\bar{3}$  structure as was speculated in Ref. [13] (“We speculate that the predicted order of the Pb-cation displacements melted at RT”). We expect that a high-precision measurement



at low temperature will confirm our prediction of the  $P\bar{1}$  structure.

Regarding the magnetic property, the measured magnetic susceptibility in Ref. [13] shows two steplike decreases at 4 and 7.8 K, more indicative of a transition into an antiferromagnetic (AFM) phase. However, our PBE +  $U$  ( $U_{\text{eff}} = 4.0$  eV) calculations show that the charge-ordering FM (CO-FM) state is slightly preferred over the charge-ordering AFM (CO-AFM) geometrical frustration state by about only 3 meV/f.u. (see Tables S4 and S5 of the SM [31]) in all three phases ( $Pn\bar{3}$ ,  $R\bar{3}$ , and  $P\bar{1}$ ). This indicates that PBE +  $U$  may not be able to accurately reproduce the magnetic ground state of the charge-ordering  $P\bar{1}$   $\text{PbCoO}_3$  structure. Thus, we calculate the energy difference between the CO-AFM and CO-FM states with the more demanding hybrid HSE functional which includes some long-range exchange. When the HSE functional is adopted, we find that the CO-AFM state is now slightly preferred (by about 5 meV/f.u.; see Table S5 of the SM [31]) over the CO-FM state, in agreement with the experimental result. Therefore, it appears that the HSE functional should be adopted to reproduce the magnetic properties of the high-pressure  $\text{PbCoO}_3$  phase with a simultaneous  $A$ -site and  $B$ -site charge ordering. We note that the charge-ordering pattern predicted from the efficient PBE +  $U$  method is reliable since the energy difference between the CO-AFM and CO-FM states (about 3–6 meV/f.u.) is much smaller than the energy difference (about 0.2 eV/f.u.) between the charge-ordering phase and the non-charge-ordering phase of high-pressure  $\text{PbCoO}_3$  (see Table S4 of the SM [31]). Now we can draw the conclusion that the high-pressure  $\text{PbCoO}_3$  phase adopts the  $A$ -site and  $B$ -site charge-ordering AFM (CO-AFM) state.

Since the HSE functional can reproduce the magnetic ground state of the high-pressure charge-ordering  $\text{PbCoO}_3$  phase, we now estimate the nearest-neighbor symmetric exchange interaction  $J$  to be 1.25 meV from the HSE results. Here, the spin interaction parameters are effective by setting the spin values of  $\text{Co}^{2+}$  to 1. By performing the PTMC simulation, there is a peak in the specific heat curve and the Néel temperature is estimated to be 15 K (see Fig. S4(c) of the SM [31]). However, in Fig. 4(f) of Ref. [13], there are two-step peaks below 10 K. Currently, we could not explain the origin of the two-peak feature. It may be due to the charge degree

of freedom and/or possible impurities that are not included in our MC simulations of the spin Hamiltonian.

#### IV. CONCLUSION

In order to efficiently search the ground state of complicated magnetic systems, we develop a powerful global optimization approach in which both structural and magnetic degrees of freedom are explicitly taken into account. With this approach, we systematically investigate the phase evolution in  $\text{PbCoO}_3$  under pressure up to 20 GPa. Our simulations give the following results: (1) structural transition from the polar  $R3c$  and  $Pna2_1$  phases to a centrosymmetric  $P\bar{1}$  phase; (2) valence transition from  $\text{Pb}^{4+}\text{Co}^{2+}\text{O}_3$  ( $R3c$  and  $Pna2_1$ ) to the simultaneous  $A$ -site and  $B$ -site charge-ordering state  $\text{Pb}^{2+}\text{Pb}_3^{4+}\text{Co}_2^{2+}\text{Co}_2^{3+}\text{O}_{12}$  ( $P\bar{1}$ ); (3) magnetic order transition from the  $G$ -type AFM order with canting magnetization ( $R3c$  and  $Pna2_1$ ) to the charge-ordering AFM order ( $P\bar{1}$ ).

The  $R3c$  phase is predicted to have a large polarization ( $96.5 \mu\text{C}/\text{cm}^2$ ) due to the cooperative coupling between the FE mode and the oxygen octahedral rotation. The ferroelectricity in the polar phase is enhanced by the unusual quadrilinear coupling of three AFE modes and the  $A$ -site FE mode. The intrinsic ME couplings in the  $R3c$  and  $Pna2_1$  phases indicate that they can be used to realize the electric field control of magnetism. The charge-ordering  $P\bar{1}$  phase is slightly different from the previously proposed  $Pn\bar{3}$  phase. Besides, this high-pressure  $P\bar{1}$  phase has a rather large band gap due to a unique pressure-induced charge-ordering mechanism. Our results suggest that pressure can induce profound phase transitions and provide a way to design alternative high-performance multiferroics, which calls for further experimental verification.

#### ACKNOWLEDGMENTS

This work is supported by NSFC 11825403, the Special Funds for Major State Basic Research (Grant No. 2015CB921700), the Program for Professor of Special Appointment (Eastern Scholar), the Qing Nian Ba Jian Program, and the Fok Ying Tung Education Foundation. We thank Dr. Y. Y. Zhang, Dr. K. Liu, Dr. T. Gu, and Dr. J. Y. Ni for useful discussions.

F.L. and W.L. contributed equally to this work.

- 
- [1] J. Wang *et al.*, *Nat. Mater.* **14**, 985 (2015).
  - [2] J. Wang *et al.*, *Science* **299**, 1719 (2003).
  - [3] K. Oka *et al.*, *J. Am. Chem. Soc.* **132**, 9438 (2010).
  - [4] T. Jia, H. Wu, G. Zhang, X. Zhang, Y. Guo, Z. Zeng, and H.-Q. Lin, *Phys. Rev. B* **83**, 174433 (2011).
  - [5] J. Buhot, C. Toulouse, Y. Gallais, A. Sacuto, R. de Sousa, D. Wang, L. Bellaiche, M. Bibes, A. Barthélémy, A. Forget, D. Colson, M. Cazayous, and M.-A. Measson, *Phys. Rev. Lett.* **115**, 267204 (2015).
  - [6] M. Guennou, P. Bouvier, P. Toulemonde, C. Darie, C. Goujon, P. Bordet, M. Hanfland, and J. Kreisel, *Phys. Rev. Lett.* **112**, 075501 (2014).
  - [7] S. Wang *et al.*, *Proc. Natl. Acad. Sci. USA* **112**, 15320 (2015).
  - [8] J. Cheng *et al.*, *Proc. Natl. Acad. Sci. USA* **112**, 1670 (2015).
  - [9] R. Yu *et al.*, *J. Am. Chem. Soc.* **137**, 12719 (2015).
  - [10] M. Azuma *et al.*, *J. Am. Chem. Soc.* **129**, 14433 (2007).
  - [11] M. Azuma *et al.*, *Nat. Commun.* **2**, 347 (2011).
  - [12] W. A. Harrison, *Phys. Rev. B* **74**, 245128 (2006).
  - [13] Y. Sakai *et al.*, *J. Am. Chem. Soc.* **139**, 4574 (2017).
  - [14] X. F. Hao, A. Stroppa, S. Picozzi, A. Filippetti, and C. Franchini, *Phys. Rev. B* **86**, 014116 (2012).
  - [15] A. A. Belik, M. Azuma, T. Saito, Y. Shimakawa, and M. Takano, *Chem. Mater.* **17**, 269 (2005).
  - [16] X. Z. Lu, X. G. Gong, and H. J. Xiang, *Comput. Mater. Sci.* **91**, 310 (2014).

- [17] P. S. Wang, W. Ren, L. Bellaiche, and H. J. Xiang, *Phys. Rev. Lett.* **114**, 147204 (2015).
- [18] X.-Z. Lu and J. M. Rondinelli, *Nat. Mater.* **15**, 951 (2016).
- [19] J. W. Guo, P. S. Wang, Y. Yuan, Q. He, J. L. Lu, T. Z. Chen, S. Z. Yang, Y. J. Wang, R. Erni, M. D. Rossell, V. Gopalan, H. J. Xiang, Y. Tokura, and P. Yu, *Phys. Rev. B* **97**, 235135 (2018).
- [20] J. S. Feng, K. Xu, L. Bellaiche, and H. J. Xiang, *New J. Phys.* **20**, 053025 (2018).
- [21] C. W. Glass, A. R. Oganov, and N. Hansen, *Comput. Phys. Commun.* **175**, 713 (2006).
- [22] Y. Wang, J. Lv, L. Zhu, and Y. Ma, *Comput. Phys. Commun.* **183**, 2063 (2012).
- [23] Y.-Y. Zhang, W. Gao, S. Chen, H. Xiang, and X.-G. Gong, *Comput. Mater. Sci.* **98**, 51 (2015).
- [24] X. Luo, J. Yang, H. Liu, X. Wu, Y. Wang, Y. Ma, S.-H. Wei, X. Gong, and H. Xiang, *J. Am. Chem. Soc.* **133**, 16285 (2011).
- [25] W. Luo, Y. Ma, X. Gong, and H. Xiang, *J. Am. Chem. Soc.* **136**, 15992 (2014).
- [26] T. Gu, W. Luo, and H. Xiang, *WIREs Comput. Mol. Sci.* **7**, e1295 (2017).
- [27] D. M. Deaven and K. M. Ho, *Phys. Rev. Lett.* **75**, 288 (1995).
- [28] G. Kresse and D. Joubert, *Phys. Rev. B* **59**, 1758 (1999).
- [29] G. Kresse and J. Fürthmüller, *Phys. Rev. B* **54**, 11169 (1996).
- [30] J. P. Perdew, K. Burke, and M. Ernzerhof, *Phys. Rev. Lett.* **77**, 3865 (1996).
- [31] See Supplemental Material at <http://link.aps.org/supplemental/10.1103/PhysRevB.99.205104> for detailed phase diagrams, band structures, MC simulations, quadrilinear couplings in phase  $Pna2_1$ , FE domains, the critical pressure of phase transitions for different  $U$ , energy difference between magnetic states, and structural parameters.
- [32] A. V. Krukau, O. A. Vydrov, A. F. Izmaylov, and G. E. Scuseria, *J. Chem. Phys.* **125**, 224106 (2006).
- [33] R. Resta, *Rev. Mod. Phys.* **66**, 899 (1994).
- [34] A. Togo, F. Oba, and I. Tanaka, *Phys. Rev. B* **78**, 134106 (2008).
- [35] P. M. Woodward, D. E. Cox, E. Moshopoulou, A. W. Sleight, and S. Morimoto, *Phys. Rev. B* **62**, 844 (2000).
- [36] A. M. Glazer, *Acta Crystallogr., Sect. B* **28**, 3384 (1972).
- [37] Y. Shi *et al.*, *Nat. Mater.* **12**, 1024 (2013).
- [38] T. Gu, T. Scarbrough, Y. Yang, J. Íñiguez, L. Bellaiche, and H. J. Xiang, *Phys. Rev. Lett.* **120**, 197602 (2018).
- [39] H. J. Xiang, M. Guennou, J. Íñiguez, J. Kreisel, and L. Bellaiche, *Phys. Rev. B* **96**, 054102 (2017).
- [40] Y.-m. Zhou, W.-t. Geng, and D.-s. Wang, *Phys. Rev. B* **57**, 5029 (1998).
- [41] I. Dzyaloshinsky, *J. Phys. Chem. Solids* **4**, 241 (1958).
- [42] T. Moriya, *Phys. Rev.* **120**, 91 (1960).
- [43] L. Bellaiche, Z. Gui, and I. A. Kornev, *J. Phys.: Condens. Matter* **24**, 312201 (2012).
- [44] N. A. Benedek and C. J. Fennie, *Phys. Rev. Lett.* **106**, 107204 (2011).
- [45] C. J. Fennie and K. M. Rabe, *Phys. Rev. B* **72**, 100103 (2005).
- [46] Y. Ma, M. Eremets, A. R. Oganov, Y. Xie, I. Trojan, S. Medvedev, A. O. Lyakhov, M. Valle, and V. Prakapenka, *Nature* **458**, 182 (2009).
- [47] J. A. Alonso, J. L. García-Muñoz, M. T. Fernández-Díaz, M. A. G. Aranda, M. J. Martínez-Lope, and M. T. Casais, *Phys. Rev. Lett.* **82**, 3871 (1999).
- [48] C. Renner, G. Aeppli, B. G. Kim, Y. A. Soh, and S. W. Cheong, *Nature* **416**, 518 (2002).